Monitoring Temperate Glacier Displacement by Multi-Temporal TerraSAR-X Images and Continuous GPS Measurements

Renaud Fallourd, Olivier Harant, Emmanuel Trouvé, Jean-Marie Nicolas, Michel Gay, Andrea Walpersdorf, Jean-Louis Mugnier, Jonathan Serafini, Diana Roşu, Lionel Bombrun, Gabriel Vasile, Nathalie Cotte, Flavien Vernier, Florence Tupin, Luc Moreau, and Philippe Bolon

Abstract

A new generation of space-borne SAR sensors were launched in 2006-2007 with ALOS, TerraSAR-X, COSMO-Sky-Med and RadarSat-2 satellites. The data available in different bands (L, C and X bands), with High Resolution (HR) or multi-polarization modes offer new possibilities to monitor glacier displacement and surface evolution by SAR remote sensing. In this paper, the first results obtained with TerraSAR-X HR SAR image time series acquired over the temperate glaciers of the Chamonix Mont-Blanc test site are presented. This area involves well-known temperate glaciers which have been monitored and instrumented i.e. stakes for annual displacement/ablation, GPS for surface displacement and cavitometer for basal displacement, for more than 50 years. The potential of 11-day repeated X-band HR SAR data for Alpine glacier monitoring is investigated by a combined use of *in-situ* measurements and multi-temporal images. Interpretations of HR images, analysis of interferometric pairs and performance assessments of target/texture tracking methods for glacier motion estimation are presented. The results obtained with 4 time series covering the Chamonix Mont-Blanc glaciers over 1 year show that the phase information is rarely preserved after 11 days on such glaciers, whereas the high resolution intensity information allows the main glacier features to be observed and displacement fields on the textured areas to be derived.

Index Terms

Synthetic Aperture Radar (SAR), High Resolution (HR), temperate glacier, motion estimation, offset tracking, corner reflector (CR)

I. Introduction

In the context of global warming, the monitoring of temperate glaciers is an important issue for economic reasons (e.g. water resources or tourism), risk assessment (e.g. falling ice or glacier lakes) and climate change monitoring. Due to the difficult access to many glacier areas and the environmental hazards, remotely sensed data are an attractive source of information to complement *in-situ* measurements [1]. Relatively few sites are instrumented in the world and it is not possible to visit every glacier regularly. Therefore, compared to sparse terrestrial ground measurements, space-borne remote sensing is expected to provide image time series, making possible regular dense measurements of physical parameters which are necessary to detect significant changes and to constrain glacier flow models. High resolution optical images have already been used to measure glacier topography and summer displacements [2]. However, winter snowfalls and clouds make optical observation impossible most of the time. SAR data are a complementary information source which has the advantage of providing images all year long.

Moreover, a complex SAR image simultaneously provides magnitude and phase information. The magnitude information (intensity images) reveals spatial features (e.g. isolated targets or textures) and temporal variation of the backscattering coefficient for various applications such as change detection [3] or snow cover analysis [4]. When the image resolution is sufficient, the intensity images are also used to measure surface displacement fields by different approaches: speckle tracking [5], offset tracking [6] and target matching [7]. Successful results have been obtained with the first generation of space-borne SAR sensors (ERS, JERS, Radarsat-1, ENVISAT satellites) over fast moving glaciers in polar regions [8]. Different texture tracking criteria have been proposed by Erten et al. to monitor temperate glaciers (Inyltshik glacier, Kirgyzstan) with ENVISAT-ASAR data [9]. The precision which can be achieved by using this information is limited by the image resolution. It is difficult to achieve precisions of greater than 1/10th of the resolution [6], so rarely less than 1 meter with the previous sensors. With the new generation of SAR sensors (e.g. TerraSAR-X or Radarsat-2) which can reach a metre resolution, a precision of about 10 centimeters can be expected.

The phase information allows phase differences (interferograms) to be computed in order to measure topography or target displacements between repeated pass acquisitions [10]. Differential SAR interferometry (D-InSAR) can measure ground deformations with a precision of a fraction of the wavelength, so a centimetric precision in C-band for instance. It has been successfully applied for glacier monitoring, especially during the ERS tandem mission where 1-day interferograms were available [11], [12]. The temporal decorrelation is the main limitation to the use of this approach, especially over temperate glaciers in the Alps: rapid surface changes of the ice in the ablation areas (several centimeters per day during the summer) and the evolution of the snow cover in the accumulation areas usually result in a decorrelation of the phase between two acquisitions separated by several days. Up to now in this area, space-borne SAR interferometry in C-band has been successful only during the cold season with 1-day interferograms [13].

After the success of the first generation of SAR satellites (ERS, RadarSat-1 and JERS), only one SAR satellite was launched during a 10-year period: ENVISAT (European Space Agency). A new generation of SAR satellites was first launched in 2006 with ALOS (Japan Space Agency), then in 2007 with TerraSAR-X (DLR, Germany), COSMO-Sky-Med (ASI, Italy) and RadarSat-2 (Canadian Space Agency).

The TerraSAR-X (TSX) SAR sensor has very different characteristic from the previous space-borne SAR: it operates in X-band (shorter wavelength than the C-band of ERS, RadarSat and ENVISAT) and offers dual-polarimetry acquisitions; the resolution can reach 2 meters in Stripmap mode and even less than 1 meter in Spotlight mode; the 11-day repeat cycle is longer than the 1-day ERS-tandem configuration, but shorter than the 35-day repeat cycle of ERS or ENVISAT satellites. The potential of SAR data for Alpine glacier monitoring strongly depends on all these parameters.

In this paper, this potential is investigated for TSX multi-temporal data by analyzing image time series acquired over the Chamonix Mont-Blanc area in the French Alps. This area has been proposed as a test-site for experimental measurements of glacier displacement and analysis of snow/firn/ice backscattering (TSX Science project MTH0232). It includes well-known glaciers such as the Mer de Glace and the Argentière glaciers which have been monitored for several decades by different scientific teams. The Argentière glacier has also been instrumented with a corner reflector (CR) provided by the DLR and a continuously recording GPS station. They were installed in the upper part of the glacier (catchment area) during the second E-SAR campaign performed over this test-site in February 2007 [14]. This ground information and the expert knowledge of glaciologists who have been studying these glaciers for many years provide the necessary “ground truth” to validate and interpret the results.

The paper is organized as follows. In Section II, a visual analysis of one year of TerraSAR-X images acquired over the Chamonix Mont-Blanc test-site is performed. The benefit of the high resolution, the interest of using moving CRs and also the rare interferometric opportunities are illustrated. This analysis shows that the intensity information is more likely to provide regular estimate of glacier displacements. In Section III, the feature/texture tracking methods used to estimate displacements in SAR images are presented and the results obtained with TSX image time series on the Argentière and the Bossons glaciers are discussed. The accuracy of these results are assessed by comparison with *in-situ* measurements. The conclusions and perspectives are drawn in Section IV.

II. One Year Analysis of TerraSAR-X Images

In the framework of the TSX science project MTH0232, 4 temporal series of TerraSAR-X complex have been acquired over the Chamonix Mont-Blanc test-site. The images have been ordered in the "SSC" format which corresponds to single look complex (SLC) images. Those images are already focused (SAR synthesis with zero Doppler), but they are still in the initial radar geometry (range and azimuth sampling). They are not geocoded since the strong distortions of SAR images in high relief areas cannot be compensated without resampling artefacts. To preserve the phase signal and the speckle statistics, it is better to perform the image analysis in the radar geometry. The geocoding is applied only at the end of the processing chain if necessary, by using lookup tables (LUT) computed by the SARLUT approach [15]. These LUTs are computed according to a digital elevation model (DEM) and provide the position of georeferenced points in the radar geometry, and vice-versa: the latitude-longitude coordinates of each SAR pixel. They have been used to compare the GPS ground truth with the SAR measurements. Table I presents the available data, their polarization mode and orbit configuration, and the number of 11-day image pairs. There are 3 series in the descending configuration and 1 in the ascending configuration. This image collection covers the studied area over 11 months (2008-09-29 to 2009-08-27).

TABLE I

Temporal series of TerraSAR-X images acquired on the Chamonix Mont-Blanc Test site.

Date	**Polarization**	**Orbit**	**Comments**
2008-09-29 to 2008-10-21	HH	Descending 5h44 UTC	2 pairs with $\Delta t = 11$ days
2009-01-06 to 2009-03-24	HH/HV	Descending 5h44 UTC	7 pairs with $\Delta t = 11$ days
2009-05-29 to 2009-08-25	HH	Descending 5h44 UTC	5 pairs with $\Delta t = 11$ days
2009-05-31 to 2009-08-27	HH	Ascending 17h25 UTC	8 pairs with $\Delta t = 11$ days

A. Contribution of High Resolution (HR)

TSX is the first civilian space-borne radar satellite providing images with a resolution close to 1 meter. The resolution depends on imaging modes. TSX sensor provides three imaging modes: Spotlight,

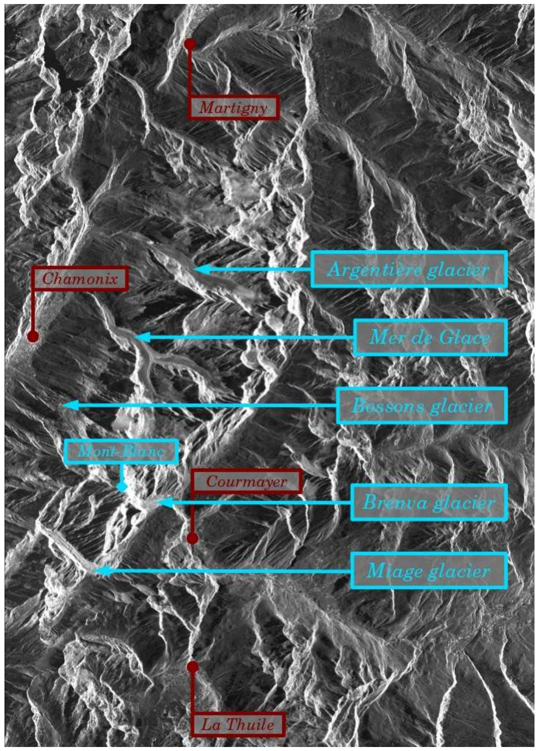

Fig. 1. TSX descending preview image of Mont Blanc test site. Positions of main glaciers studied in this paper.

Stripmap and ScanSAR [16]. The Stripmap mode has been chosen because it provides wider coverage (i.e. 30 km$\times$50 km in range and azimuth directions respectively) and high resolution (about 2 meters). With this mode, all the Mont-Blanc test site is covered (see Fig 1), whereas the coverage of the very high resolution Spotlight mode is limited; it can only image about 10 km in azimuth direction, limiting the spatial coverage of glaciers in the region. The ScanSAR mode supplies larger scene coverage than the Stripmap mode, but with a lower resolution (about 16 meters in azimuth and 2 meters in range).

In the 4 Stripmap time series of TSX images, the best ground projected pixel spacing is respectively 2.0 m in azimuth and 2.2 m in range in single polarization mode. With such precision, it is possible to see more details than with previous space-borne SAR sensor images. As illustrated in Fig. 2, it is easy to discriminate between non-crevassed and crevassed parts, ablation and accumulation areas on the Argentière glacier. In amplitude images, zones with crevasses appear as succession of shadows and bright lines. The accumulation area, with high density snow, appears with a stronger backscattering coefficient than the ablation area. The two CRs which are installed in the upper part of the Argentière glacier are visible in the intensity images (see Fig. 6). The first CR which was installed by the DLR in February

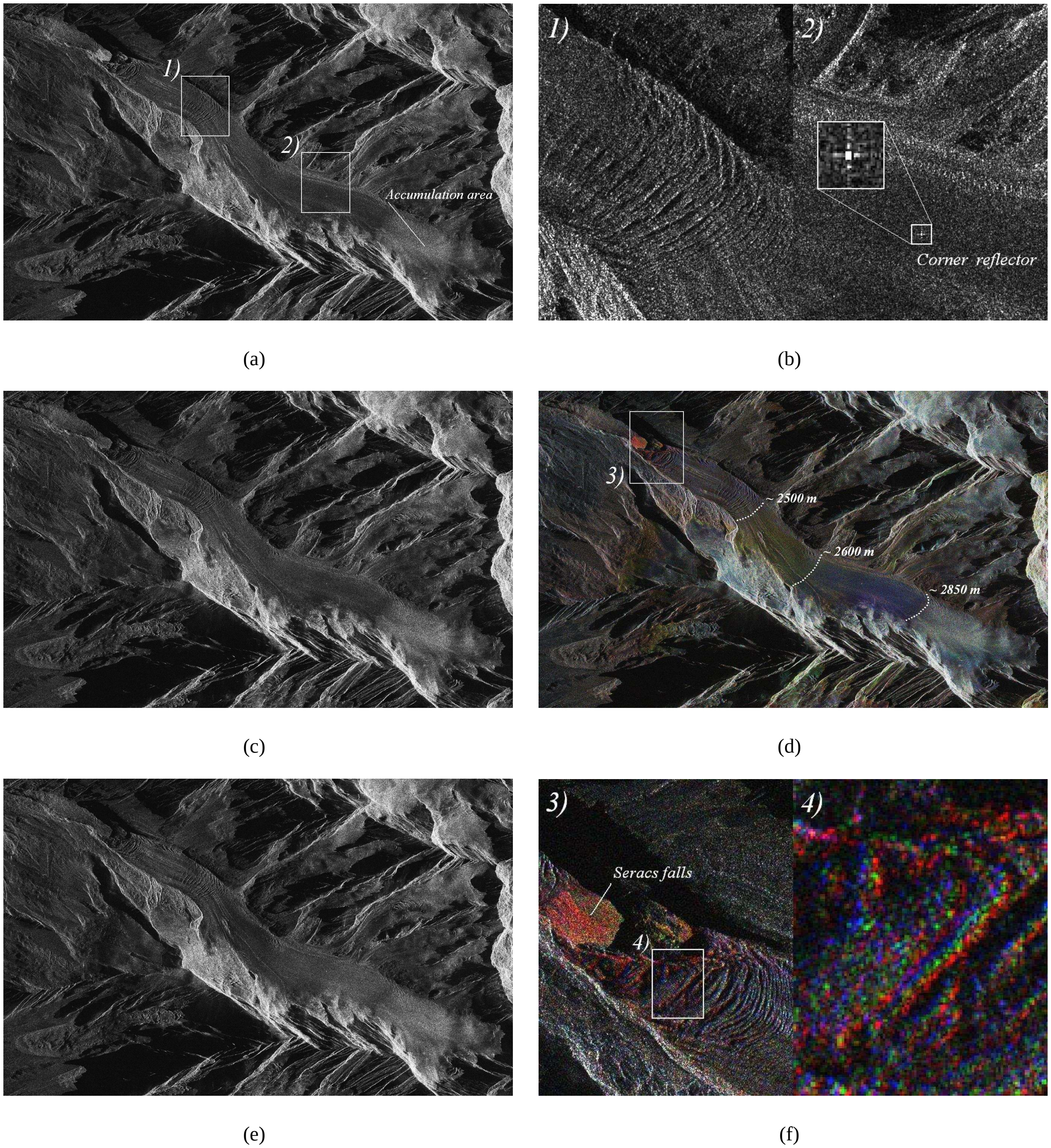

Fig. 2. **Descending amplitude TerraSAR-X images of the Argentière glacier: (a) 2008-09-29, (c) 2008-10-10, (e) 2008-10-21 and (b) zoom on crevasses *(1)* and CR *(2)*; (d) Red(2008-09-29)-Green(2008-10-10)-Blue(2008-10-21) color composition and (f) zoom on "Lognan serac falls" *(3)* and red-green-blue fringes caused by glacier displacement *(4)*.**

2007 [14] is configured for descending tracks, whereas the second CR, installed by EFIDIR team in May 2009, is configured for ascending tracks. Their intensities are about 40 dB and 25 dB higher than the

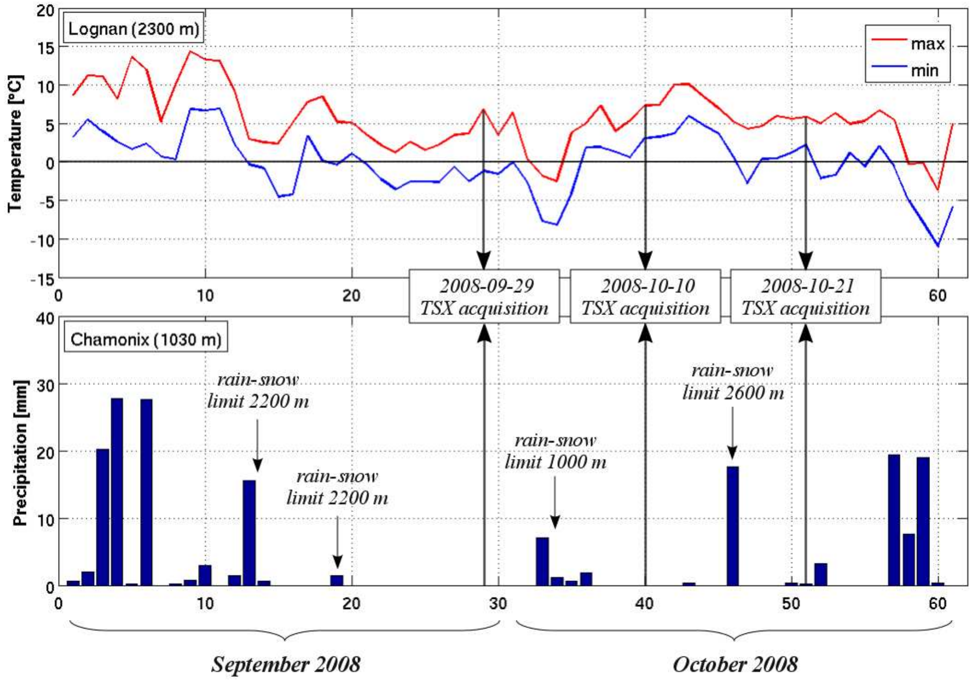

Fig. 3. September - October 2008 meteorological conditions over the Chamonix Mont-Blanc test site; Tempartures came from the Lognan (2300 m) LGGE station and precipitations from the Chamonix (1030 m) Météo-France station.

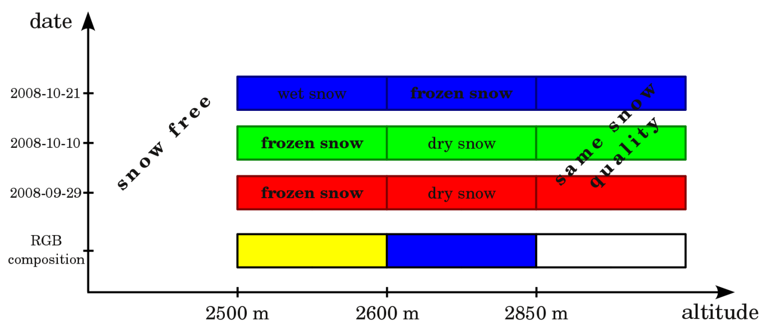

Fig. 4. Snow cover evolution on Argentière glacier according to the altitude for the three acquisitions used in the RGB composition (see Fig. 2). The bold type denotes the snow with the stronger backscattering.

local mean, for descending and ascending CRs respectively. Their different size explains this intensity difference (Fig. 5).

Temporal evolutions can be observed by computing Red-Green-Blue (RGB) compositions with 3 amplitude images acquired at different dates. These compositions reveal specific features such as serac

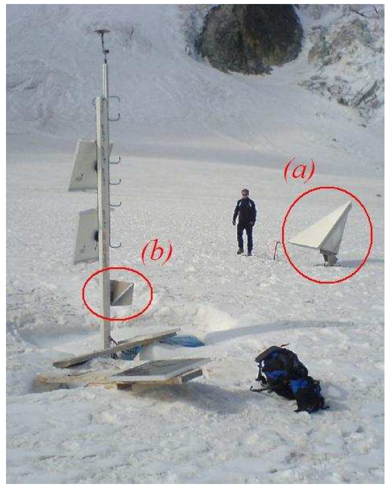

Fig. 5. CRs and GPS on the Argentière glacier. (a) Descending CR (1.5 m height), 5 m from the GPS station; (b) Ascending CR (0.3 m height), fixed on the GPS mast.

falls or fast moving crevasses, and also important radiometric variations due to surface changes such as snow falls and melting/freezing periods.

A RGB composition of the Argentière glacier made with the autumn-2008 time series is presented in Fig. 2-(d). A typical serac falls area just below the level of ”Lognan serac falls” can be observed in Fig. 2-(f). Serac falls generate areas with ice blocks which increase the ground roughness and the backscattered signal. This area appears in red because of a serac fall which took place before 2008-09-29. Then, on two next dates, 11 and 22 days later, the backscattering decreased because of the ice blocks melting and settling. The fast moving parts of the glacier with crevasses are also highlighted by the color composition of high resolution images. They create red-green-blue pseudo-fringes which can be observed in Fig. 2-(f).

The RGB composition also emphasizes the surface change in the upper part of the Argentière glacier (Fig. 2-(d)): blue and yellow areas just below the accumulation part. These changes are due to the meteorological events during September and October 2008, which are reported in Fig. 3. The snow falls often first reduce the SAR backscattering, especially in X band. After a while, depending on the night/day temperatures at the different elevation, the snow becomes either wetter with even lower backscattering, or frozen close to the surface, which increases the backscattering [17]. The TerraSAR-X descending images used for this color-composition have been acquired early in the morning, in a period where the temperatures are often negative during the night and positive during the day. This can explain the behavior

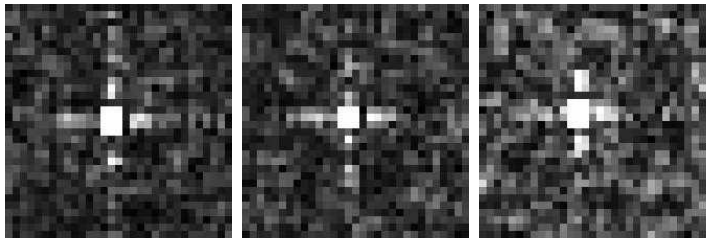

(a) 2009-09-29 (b) 2009-10-10 (c) 2009-10-21

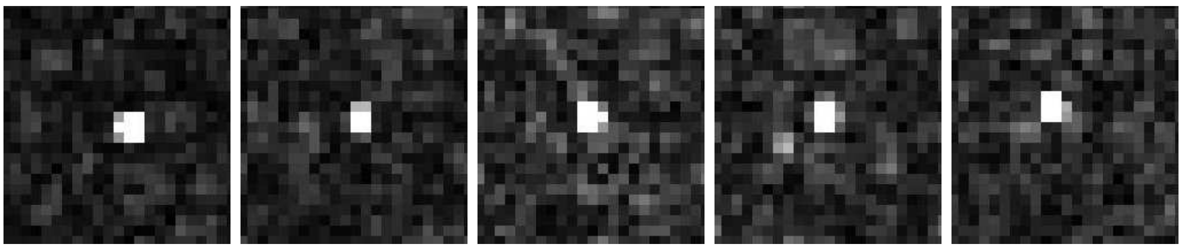

(d) 2009-05-31 (e) 2009-06-11 (f) 2009-06-22 (g) 2009-07-03 (h) 2009-07-14

Fig. 6. Amplitude images of two CRs fixed in the upper part of the Argentière glacier: (a)-(c) descending DLR CR (Fig 5-(a)); (d)-(h) ascending EFIDIR CR (Fig 5-(b)).

of the 4 different parts as summerized in Fig. 4:

- Below 2500 m, the glacier surface is free of snow at the 3 dates: the September snow falls and the weak snow falls between 2008-10-03 and 2008-10-06 (snow-rain limit at about 1000 m) were followed by warmer weather which removed the snow up to 2500 m high. The similar backscattering levels of the 3 images do not produce any color.
- Between 2500 m and 2600 m, the glacier surface is probably covered by snow which has started to melt during the day and become frozen during the night in the 2008-09-29 and 2008-10-10 images, and by wet snow in the 2008-10-21 image. The yellow color results from the increased intensity in red (2008-09-29) and green (2008-10-10) images.
- Between 2600 m and 2850 m, the glacier surface is probably still covered by dry snow in the 2008-09-29 and 2008-10-10 images. In the 2008-10-21 image, the recent snow from 2008-10-16 (snow-line at about 2600) is likely to have started to melt and freeze, creating a stronger backscattering than in the previous images, which yields to a blue color.
- Above 2850 m, approximately the equilibrium line, the recent snowfalls and the firn from the previous year generate rather strong backscattering coefficients similar in the 3 images. This results in the white area visible in the upper part of the glacier.

B. D-InSAR potential

According to preliminary studies, TSX D-InSAR measurements on temperate glaciers are quite difficult because of the X-band sensitivity to ground surface roughness, and glacier surface changes during the 11-day interval of TSX repeat orbit [18][19]. The high resolution of the TSX images should improve the possibility of finding valid interferometric pairs, depending on the surface cover and the registration accuracy on the moving parts. For example, a temperate glacier like Argentière presents a large number of stones in some areas and can move approximately 2 m/11 days. Considering the data collection presented in Tab. I, it is possible to make 22 interferometric pairs with temporal baseline of 11 days: 2 in autumn 2008, 7 in winter 2009 and 13 in spring/summer 2009. The cold season is more likely to provide the best D-InSAR results because of reduced surface changes. Nonetheless, for the TSX sensor, the X-band is sensitive to snowfalls and snow settling due to gravity and spell of milder weather.

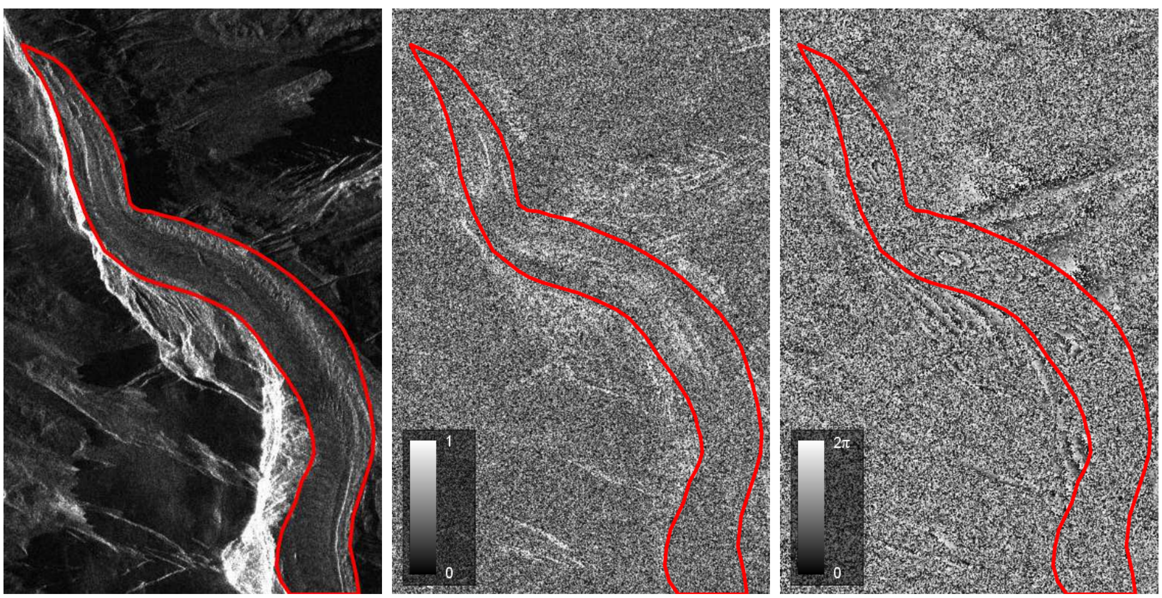

(a) (b) (c)

Fig. 7. TSX 11-day pair (2009-01-06/2009-01-17) over the Mer de Glace glacier. Average amplitude (a), InSAR coherence (b) and phase (c) processed with 4×7 multi-looking, baseline $B_{\perp}$ = 38 m.

As expected the interferometric pairs of autumn 2008 and spring/summer 2009 show that the coherence is lost over the the Argentière and Mer de Glace glaciers whereas high coherence level parts can be found in surrounding areas without snow/ice and forest cover. In autumn, several parts of ”black” glaciers (surfaced by stones) such as the Miage and the Brenva glaciers present relatively high coherence, and useful phase information. In addition of the debris covered surface, the relatively slow displacement of the

Miage glacier lower part (60 m/an) its the reason why this local coherence preservation can be observed in the middle of a non-moving area without a specific registration. Among the 7 interferometric pairs of winter 2009, only one works (2009-01-06/2009-01-17) over the middle part of the Argentière glacier and also over the lower part of the Mer de Glace (see Fig 7). A long period with anti-cyclonic weather and cold temperatures led to this result. Furthermore, those coherent parts coincide with stones on the glacier surface. On the contrary, all other InSAR pairs do not work because of snowfalls and several spell of milder weather in February and March 2009.

C. First conclusions

Visual inspection shows the high resolution and quality of TSX Stripmap image details. Compared to previous SAR sensors, the HR improves the potential of SAR imagery for glacier monitoring as illustrated by RGB images. Most of the interesting features are clearly visible and a visual tracking of the glacier displacement is possible. Some image animations can be seen on the EFIDIR project web-site [20].

Regarding the TSX D-InSAR measurement potential over those temperate glaciers, with 8 images acquired in winter 2009, only a single valid interferometric pair has been obtained. Preserving the phase information requires too specific conditions to perform regular measurements: for example no snowfall, long period (11 days) with anti-cyclonic weather and cold temperature. In the French Alps, it is rare to have such meteorological conditions longer than one week. Up to now, it seems difficult to obtain interferometric series over alpine temperate glaciers with TerraSAR-X images because of its 11-day repeat orbit and the French Alpine winter climate. In the future, TanDEM-X data with single pass interferometry will overcome the coherence limitation and provide accurate DEM over the glacier as well as surrounding mountains. One may expect to follow glacier surface elevation changes and use this information as input for glacier monitoring.

In conclusion, to monitor Alpine glacier displacements with TSX images, it is better to use alternative methods to D-InSAR. According to the visibility of small size CRs and of the fast parts of the glaciers with crevasses in TSX meter resolution images, it is interesting to explore the potential and limitations of target/surface offset tracking methods.

III. ESTIMATION OF THE GLACIER DISPLACEMENTS

The previous analysis of the TSX data (Sec. II) shows that it is necessary to track the two types of target encountered in SAR images: point targets (artificial such as CRs or natural such as large rocks) and distributed targets where the backscattered signal is not dominated by a single scatterer. This signal is the sum of the responses of elementary targets distributed over the surface (or the volume) contributing to the pixel. The speckle effect which results from this sum makes the tracking of hidden texture or partly visible features more difficult. Accordingly, two different approaches are used to retrieve the displacement information: one dedicated to point targets and one for distributed targets which can also be tested on point targets. This section first recalls their principles, then describes the two sources of *in-situ* measurements and finally presents the results obtained over two glaciers of the Chamonix Mont-Blanc test-site.

A. Methods used for displacement estimation

1) Point target measurements: In 2006, Francesco Serafino developed a new method to estimate displacement in SAR imagery [7]. This technique consists in exploiting the backscattered signal of isolated and bright points (named IPS for Isolated Point Scatterer) to find their local shifts. The aim of the method is to apply the match filter between the ideal impulse response of the system and some IPS. The typical impulse response of SAR sensor is a double cardinal sinus in range and azimuth directions:

$$I_{sinc}(x_{LOS}, y_{az}) = \text{sinc}\left(\frac{x_{LOS}}{\delta_{LOS}}\right) \cdot \text{sinc}\left(\frac{y_{az}}{\delta_{az}}\right) \tag{1}$$

where $\delta_{LOS} = \frac{c}{2KT}$ and $\delta_{az} = \frac{L}{2}$ are the range (LOS) and azimuth resolutions, and $(x_{LOS}, y_{az}) = (az_{px} \cdot i,\ rg_{px} \cdot j)$ with the usual notations ((i, j): pixel local coordinates, K: chirp constant, T: chirp duration, c: speed of light, L: antenna length, rg_{px} and az_{px}: range and azimuth pixel spacing). For specific targets such as CRs, the side-lobes of the 2D "sinc" function can be observed in the SAR images as illustrated in Fig. 6-(a-c).

The displacement estimation procedure can be divided into two steps : the IPS selection and the sub-pixel shift estimation. For the first step, the IPS selection is carried out by evaluating the cross-correlation function between the SAR image and a truncated version of the ideal bidimensional impulse response. In practice, the images are over-sampled by a factor of two in range and azimuth directions. Then, a scatterer is considered as IPS if the cross-correlation value is larger than a fixed threshold and if no other scatterers are detected in its neighborhood. Concerning the second step, the sub-pixel position in range and azimuth is computed for each IPS in the master and slave SAR images. The IPS position is obtained by finding the coordinates of the cross-correlation maximum value between the patch and the truncated ideal impulse response. Then, the estimated shift is obtained by subtracting the sub-pixel IPS coordinates in range and azimuth for the two SAR acquisitions. In the following part of the article this method is called sinc method.

2) Distributed target measurements: A conventionnal approach is used to measure the displacement of distributed targets between two images. This approach consists in defining a spatial neighborhood for a pixel of the first image, and searching the location of the most similar configuration in the second image. This approach, also called offset tracking, is applied here to estimate the displacement field between two intensity images: the master image $I_m\,(i,j)$ and the slave image $I_s\,(i,j)$, after an initial registration on the motion-free parts of the images. For a pixel (i,j) in the master image, the displacement vector $\vec{V}\,(i,j)$ is obtained by computing the values of a similarity function $sim(p,q)$ between a master block Ω_m centered in pixel (i,j) and the same block Ω_s translated by (p,q) in the slave image. According to a-priori displacement information, the search is made for $(p,q) \in \Delta = [p_{min}, p_{max}] \times [q_{min}, q_{max}]$. The displacement vector estimated in pixel (i,j) is:

$$\vec{V}^d\,(i,j) = (p_{opt}, q_{opt}) = \underset{(p,q)\in\Delta}{Argmax}\; sim\,(p,q) \tag{2}$$

where (p_{opt}, q_{opt}) is the offset which maximize the similarity function $sim\,(p,q)$. The resulting displacement measurement based on this optimal position is discreet: (p_{opt}, q_{opt}) are integer numbers and the displacements values are multiples of the pixel spacing.

To improve the precision, a sub-pixel measurement $\vec{V}^{sub}\,(i,j)$ is computed in two steps. First, the similarity function $sim(p,q)$ is approximated by a second order polynomial function near the position (p_{opt}, q_{opt}) over the 3×3 block $[p_{opt}-1, p_{opt}+1] \times [q_{opt}-1, q_{opt}+1]$. Secondly, the sub-pixel position of the $sim\,(p,q)$ function maximum is obtained by cancelling the first derivatives of the interpolated function in azimuth and range directions. Finally, using the pixel spacing in range and azimuth and the temporal interval Δt between master and slave images, the magnitude and the orientation of the displacement vector are calculated in cm/day and degrees respectively.

In this paper, two different similarity functions have been tested: a conventional one, the Zero-mean Normalized Cross-Correlation (ZNCC), and a criterion specific to SAR images: the uncorrelated maximum likelihood (UML) criterion proposed by Erten and al. [9]. The maximisation of the correlation function corresponds to the minimization of the squared difference between Ω_m and Ω_s sub-images. This criterion has been applied for image co-registration [21] or displacement measurements from optical data [2] or SAR images [8]. It is well-suited to images corrupted by additive noise and is not always robust enough to monitor displacements in SAR images corrupted by speckle.

The ZNCC similarity function is defined as:

$$ZNCC\left(p,q\right)=\frac{\sum\limits_{(k,l)\in\Omega_m}\left(I_m\left(k,l\right)-\overline{I}_m\right)\left(I_s\left(k+p,l+q\right)-\overline{I}_s\right)}{\sqrt{\sum\limits_{(k,l)\in\Omega_m}\left|I_m\left(k,l\right)-\overline{I}_m\right|^2\sum\limits_{(k,l)\in\Omega_m}\left|I_s\left(k+p,l+q\right)-\overline{I}_s\right|^2}} \qquad (3)$$

where $\overline{I}_m$ and $\overline{I}_s$ denote the mean over Ω_m and Ω_s respectively.

The offset tracking approach proposed by Erten *et al.* takes multiplicative noise statistics of SAR imagery into account. This UML similarity function which direved from maximum likelihood approach is defined as:

$$UML\left(p,q\right)=\sum_{(k,l)\in\Omega_m}\left(\underline{I}_m\left(k,l\right)-\underline{I}_s\left(k+p,l+q\right)-2\ln\left(1+e^{\left(\underline{I}_m(k,l)-\underline{I}_s(k+p,l+q)\right)}\right)\right) \qquad (4)$$

where $\underline{I}_m=\ln\left(I_m\right)$ and $\underline{I}_s=\ln\left(I_s\right)$. The UML function is derived under the hypothesis of Gamma distributed speckle noise and uncorrelated speckle between the 2 images. In regards to Chatelain *et al.* [3], this hypothesis is valid when the ZNCC value are below 0.5. The maximization of the ZNCC function between two intensity SAR images on the Argentière and the Bossons glaciers (Fig.9 and Fig. 10), shows that in this data set, the speckle is decorrelated after 11 days on the glacier surfaces, which also confirms that D-InSAR technique cannot be applied.

B. In situ measurements

Since summer 2007, four continuous GPS stations have been recording in the Argentière glacier area:

- station n°1, in the upper part of the glacier (alt. 2767 m), close to the DLR and EFIDIR CRs (see Fig. 5),
- station n°2, on the bedrock beside the glacier (alt. 2837 m), close to the Argentière refuge,
- station n°3, in the middle part of the glacier (alt. 2360 m), just before the Lognan serac fall,
- station n°4, down in the valley (alt. 1121 m), in the town of Chamonix.

For the three time series presented in this work, autumn 2008 (descending track) and spring/summer 2009 (descending and ascending tracks), stations n°1, n°2 and n°4, were operational. Station n°3 was only operating during the spring/summer 2009 acquisitions. The GPS data of those three stations have been combined with continuous GPS data of 42 stations from the French RENAG and RGP and the European EUREF networks (http://renag.unice.fr, http://rgp.ign.fr, http://www.euref-iag.net/) and analyzed with the GAMIT/GLOBK software created at MIT [22]. The data are acquired at a 30 sec interval. The station coordinates are estimated over 6-hour sessions. This results in position time series with four estimates per day. The positioning of the fast moving glacier site with respect to the stable reference stations is estimated with formal uncertainties of 2-3 mm on the horizontal components and 9-11 mm on the vertical component for each 6-hour session. Those positions can be used to determine a linear displacement rate over the total observation span (18 days for the glacier sites missing the last four days), or over sub-intervals between the successive satellite image acquisition dates. In a second analysis step tropospheric parameters are estimated with a high temporal resolution (one zenith tropospheric delay every 15 min). Here a sliding window strategy is used shifting 8 six-hour sessions per day by 3 hours and keeping only the results from the central 3 hour interval of each solution.

C. Results on the Mont-Blanc test site

1) Result description: This study is performed with autumn 2008 descending time series and spring/summer 2009 descending and ascending time series (see Tab. I). During those time periods, the CRs are visible. All results are calculated with 11-day image pairs. A larger temporal interval Δt increases the decorrelation on the glacier and reduces the measurement confidence as illustrated in Fig. 8-(a). With a temporal distance $\Delta t = 11$ days (Fig. 8-(b)), the ZNCC value is relatively constant and stay close to 0.3 in the summer period. The window size used for ”distributed target” approach depends on the morphological caracteristics of the tracked features for the Ω_m block size, and on the magnitude of the displacement for the Δ exploration size. When point targets are tracked, Ω_m should be relatively small. For CR tracking, the Ω_m block used is 31×31 pixels large, about 70 m and 62 m in ground range and azimuth direction. When glacier surface features are tracked, Ω_m can be larger in order to increase the chance of including natural structures or textures [23]. For the Argentière glacier, with a surface only partially covered with debris and only two crevasse areas, the Ω_m block used is 101×101 pixels large, about 228 m and 202 m in ground geometry. For the Bossons glacier, with a surface mostly covered with the structures due to crevasses, the Ω_m block can be reduced to 61×61 pixels, about 124 m and 83 m in ground geometry.

The initial image registration is made on motion-free areas by a translation without applying sub-pixel offsets. This avoids the resampling of the slave image with a blurring effect due to the pixel interpolation. The disadvantage is that it can introduce up to 0.5 pixel co-registration error, and even more in the range direction when the elevation changes. This effect depends on the orbit perpendicular baseline and on the glacier topography. These co-registration errors have been corrected by two different strategies:

- In the azimuth direction, the co-registration is not affected by the topography at the glacier scale. In this case, the remaining azimuth co-registration offset is estimated by the sub-pixel ZNCC technique over motion-free areas near the glacier. The distribution of these azimuth offsets has a high narrow

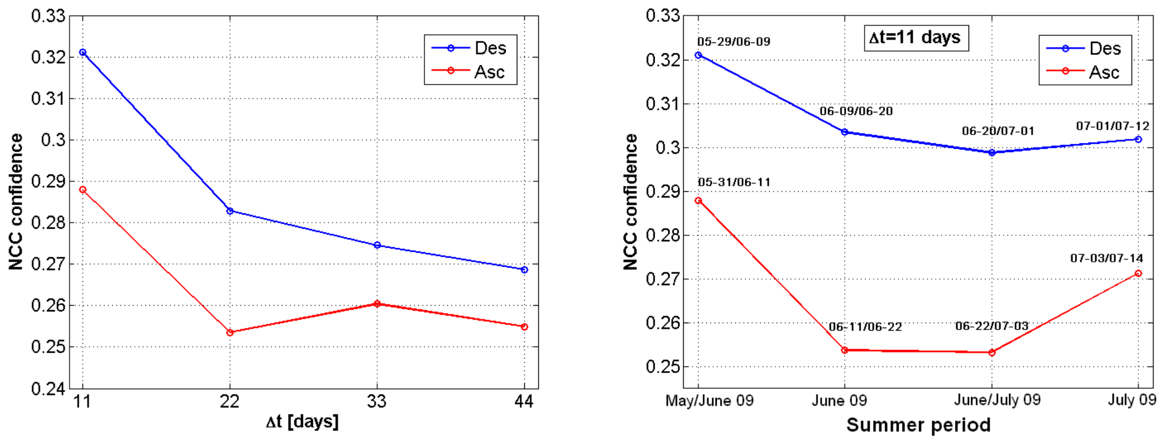

(a) (b)

Fig. 8. Evolution of the ZNCC on the lower part of the Argentière glacier (the most correlated part) according to track configuration and temporal interval Δt: (a) pairs with Δt varying from 11 days to 44 days and (b) pairs with Δt =11 days during the summer period.

mode. The modal value can be easily computed and provides the azimut offset correction.

- In the range direction, the topography of the studied area can create offset variations greater than 2 pixels between the lower and the upper part of the glaciers. To separate the sought-after displacement information from this stereo effect, it is necessary to compute the range variations between the two images by using a DEM and precise orbit interpolations. The DEM used in this study has been computed from airborne photography acquired by the French Geographic National Institute (IGN). The 5-meter contour lines provided by the ”Régie de Données 73-74” [24] (geographic data local agency) have been transformed into a raster DEM with 10-meter pixel spacing by using ARC-GIS software. Regarding the TerraSAR-X orbits, the state vectors have been interpolated with a 1-meter step to compute the antenna/DEM distance which is used for the geocoding and the computation of the range distortions due to the topography [15]. This provides the remaining local range co-registration error to be corrected after the estimation of the displacement. The accuracy of this technique has been verified by comparing the range offsets derived from the orbits with the sub-pixel ZNCC offsets on motion-free well-correlated areas.

All displacement results are expressed in cm/day in the two-dimension (2D) SAR geometry, since the SAR measurements provide only the projections of the true 3D displacements in the azimuth/range (line of sight) directions. Consequently all *in-situ* measurements, expressed in three dimensions (North,East,Up), are converted in SAR geometry (see Appendix-A). Therefore the comparison is possible without introducing any hypothesis such as surface parallel flow to build 3D vectors from the 2D SAR measurements. To assess performances, SAR measurements and the projected in situ measurements considered as ”ground truth” are compared by computing magnitude and orientation errors. The magnitude errors correspond to the magnitude of the error vector (the difference between the ”ground truth” and the SAR displacement vectors). The orientation errors correspond to the angle between the SAR displacement vector and the ground truth vector. Then the Root Mean Square (RMS) error is calculated for each time series and for all the time series (Total RMS error).

2) General analysis: The global displacements of the Argentière and the Bossons glaciers computed with the ZNCC similarity function are shown in Fig. 9 and Fig. 10 respectively. The ZNCC value can be used as a confidence measure to select the pixels where the similarity is high enough. The results are presented with a grey mask preserving the areas where the ZNCC value is higher than a threshold set to 0.2 as in [8]. The displacement estimation of the Bossons glacier (Fig. 10) shows typical displacement patterns of the glacier with the highest displacement in the center of the glacier and a gradient towards the boundary (see Fig. 11-(a)). The two zones with the largest displacements correspond to an increase of the slope (see Fig. 11-(b)). The major part of the Bossons glacier surface is mapped with a ZNCC value higher than 0.2. This good result is due to the crevassed surface of this glacier. Conversely, the major part of Argentière glacier (Fig. 9) is not mapped. Only the CR and the two crevassed areas provide a correct displacement estimations with ZNCC value higher than 0.2. The largest glacier displacement can be observed before the ”Lognan serac falls” where the basal topography creates a slope break. The tests carried out with the other Argentière time series, including ascending pairs, show the same results.

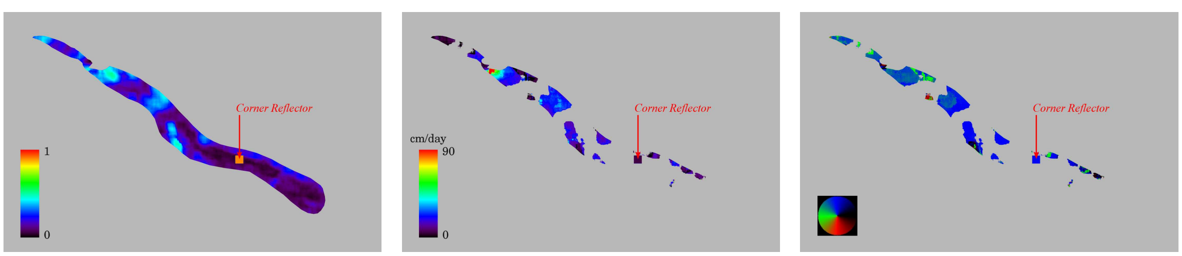

(a) (b) (c)

Fig. 9. ZNCC displacement estimation of the Argentière glacier computed with 2008-09-29/2008-10-10 pair. Value of ZNCC maximization (a), magnitude (b) and orientation (c) of displacement estimation vector.

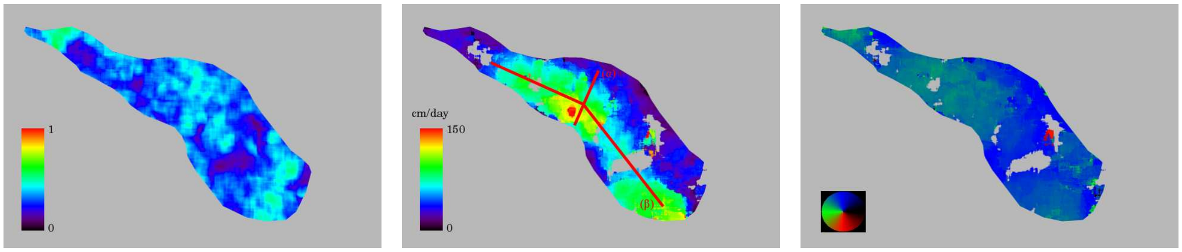

(a) (b) (c)

Fig. 10. ZNCC displacement estimation of Bossons glacier computed with 2008-09-29/2008-10-10 pair. Value of ZNCC maximization (a), magnitude (b) and orientation (c) of displacement estimation vector.

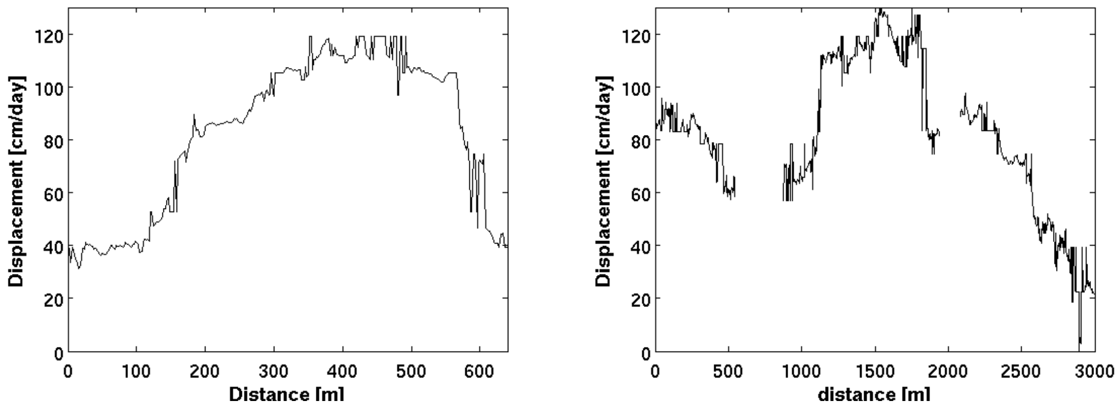

(a) (b)

Fig. 11. Displacement profile measurements using Bossons glacier displacement map (Fig. 10-(b)) : (a) transverse profile (profile α) and (b) longitudinal profile (profile β).

3) GPS comparison: The results obtained by the point target measurement (sinc) and the distributed target methods (ZNCC and UML) are compared with the GPS measurements provided by station n°1 at 2767 m (Tab. II) and station n°3 at 2360 m (Tab. III). Tab. II shows that the sinc method gives the best RMS error for orientation and that the ZNCC method gives the best RMS error for magnitude. The ZNCC performance is close to the sinc performance, whereas the UML method shows the worst results. This can be explained by the UML hypothesis of fully developed speckle which corresponds to distributed targets and makes this method inappropriate for point target measurements.

Regarding the track configuration, descending time series present better results than ascending time series. There are probably two reasons. The first one is the difference between the two CRs visible in Fig. 5. The descending CR provided by the DLR is about 4 times bigger than the small CR built by the EFIDIR laboratories to complement the experiment for ascending images. Moreover, the DLR CR includes a specific foot to adjust precisely the orientation and elevation in the radar line of sight, whereas the small CR is installed on a vertical mast and oriented “as well as possible”. CR size and orientation precision impact the signal/clutter ratio and the patterns due to the CRs in amplitude images (cf. Fig. 6): the “cross” due to the 2D sinc function appears clearly for the large DLR CR whereas only the main lobe peak can be detected for the small CRs. This affects the precision of the results obtained by the correlation of these patterns (either between two SAR images for the ZNCC method, or with the theoretical impulse response for the sinc method) and reduces the accuracy of ascending small CR measurements compared to descending ones. A second reason could be the time of the day which is different for ascending and descending images. Descending images are acquired early in the morning (5h44 UTC) whereas ascending images are acquired in the evening (17h25 UTC). In the morning, the atmosphere is rather stable in this mountainous area whereas storms or precipitations often occur at the end of the day, especially during the summer season. Accordingly, evening ascending images are more likely to be affected by atmospheric perturbations, which create path differences usually observed in SAR interferograms and also localization errors (up to 20 cm as reported in [25]). However, these results show that it is possible to measure the displacement with a low-cost foldable CR, making this experiment rather easy to be reproduced.

To complement this study and to collect “ground truth” data with a higher temporal resolution than the annual measurement performed on ablation stakes, another EFIDIR CR (a twin CR with a CR oriented for ascending passes and one for descending passes) has been installed in the middle part of the glacier near GPS station n°3 at 2360 m. The SAR measures obtained on these artificial targets and on the natural glacier surface in this area, are compared with the GPS measures in Tab. III.

For the CRs, the magnitude RMS and orientation errors are higher than with the CRs installed in the upper part of the glacier. But the GPS data from station n°3 are less precise than usual because of the difficulties encountered with this station. The antenna was first installed on a mast which fell on 2009/06/17 because of the strong ablation rate. It was then reinstalled on a large stone, but this stone has its own motion due to sun and shadow differences around the block. Despite the different sources of uncertainty, one can notice that the comparison of the 4 mean displacements (3 in Tab. II, 1 in Tab. III) shows a good agreement between the SAR CR technique and the GPS measures.

For natural textured areas, the ZNCC and UML results are rather close (less than 1 cm difference in magnitude and less than 3° difference in orientation), except for the 2009-07-14/2009-07-25 pair where the UML result is erroneous. Such large error could be avoided by taking a simple model of the glacier flow into account and using it as prior information. The difference with the displacement of the GPS station n°3 is larger than with the artificial targets and increases in August. This probably comes from the location which is different from the GPS and CR location to avoid the influence of the CR response in the estimation window, and from the “rotation” of the block where the GPS antenna was fixed due to the hight temperature of August 2009.

IV. Conclusions and Perspectives

In this paper, the early results obtained with multi-temporal TerraSAR-X images over the Chamonix Mont-Blanc glaciers have been presented and compared with in-situ measurements.

Regarding the phase information, the analysis of several autumn and winter 11-day interferograms shows that, on white glaciers (ice/snow covered), surface changes are of excessive magnitude to regularly obtain coherence and phase information, whereas on black glaciers (covered by stones), or in intermediate areas, the coherence can be high enough to observe displacement fringes. However, the moving parts of such glaciers have to be carefully registered in order to preserve this information: with TSX HR data on fast moving glaciers, the global registration obtained on non-moving well-correlated areas may result in important mis-registration over the glacier. The use of prior information on the glacier location and displacement should be investigated to respond to this specific requirement on sparse, poorly correlated, moving areas.

Regarding the intensity information, the gain in resolution makes the observation of Alpine glaciers important features feasible: for example large stones, crevasses and seracs. Due to their increased visibility and the meter resolution, the displacement of fast-moving glaciers can also be measured on the intensity image by ”correlation like” methods. Two different kinds of features have been successfully tracked: point target features with artificial targets (moving corner reflectors) and natural texture features. Those results have been compared with in-situ measurements (continuous GPS located near the corners). They show that both approaches are feasible and complementary: the displacement estimation by texture tracking on textured areas, such as crevassed areas or in the presence of stones, and the detection and accurate localization of isolated point targets created by corner reflectors. The conventional ZNCC method is not specific to SAR images. However, it provides results which are close to those obtained by two methods recently proposed for SAR images: the sinc method for point targets and the UML method for distributed targets. The sinc method can be applied only on isolated point targets and is rather efficient for corner reflectors. The UML method can be applied over the whole image. However, satisfactory results are obtained only on speckled textured areas and not on isolated point targets.

The ZNCC method has the advantage to make a single analysis possible for both kind of features and to provide a reliable confidence measure (the correlation level) to discard unreliable results. Finally, for this application, it is preferable to use images acquired early in the morning than late in the afternoon, especially during summer, since atmospheric perturbations are more likely to affect the evening images, creating geolocalization and displacement measurement errors.

Some further work is necessary to refine the different methods using multi-temporal SAR images in order to derive displacements with higher accuracy and to assess the uncertainty of the different approaches. It will include the fusion of the different information sources, especially a combined use of SAR and GPS data. Since the GPS tropospheric delays are equivalent to the tropospheric delays affecting the satellite radar images, the GPS network can be used to correct this persistent error in SAR imagery. The tropospheric variability in the atmospheric layers observed by our GPS stations (1121m-2767m and 2767m-2837m) offers interesting perspective for the development of SAR tropospheric corrections from GPS observations.

Appendix A
Projection of in-situ measurements in SAR geometry

The ground measurements (GPS or stakes) of the glacier displacement vector $\vec{V}_{gnd}^{3d}$ are made in three dimensions in conventionnel East, North, Up basis $\mathcal{B}_{3d} = (O, \vec{u}_e, \vec{u}_n, \vec{u}_u)$ (see Fig. 12):

$$\vec{V}_{gnd}^{3d} = \begin{bmatrix} V_e \\ V_n \\ V_u \end{bmatrix} \tag{5}$$

In the SAR image, the measurement of the glacier displacement vector $\vec{V}_{sar}^{i}$ is made in two dimensions in orthonormal basis $\mathcal{B}_{SAR}^{i} = (O, \vec{u}_{los}^{i}, \vec{u}_{az}^{i})$ with $i \in \{descending, ascending\}$:

$$\vec{V}_{sar}^{i} = \begin{bmatrix} V_{los}^{\ i} \\ V_{az}^{\ i} \end{bmatrix} \tag{6}$$

where $V_{los}^{\ i}$ and $V_{az}^{\ i}$ correspond to the projection of the displacement, respectively in line of sight (range) and azimuth directions.

Then, the projection $\vec{V}_{gndtoSAR}^{i}$ of *in-situ* measurements in the SAR geometry is computed by the scalar product between $\vec{V}_{3d}^{gnd}$ and $(\vec{u}_{los}^{i}, \vec{u}_{az}^{i})$:

$$\vec{V}_{gndtoSAR}^{i} = \begin{bmatrix} \vec{V}_{3d}^{gnd} . \vec{u}_{los}^{\ i} \\ \vec{V}_{3d}^{gnd} . \vec{u}_{az}^{\ i} \end{bmatrix} \tag{7}$$

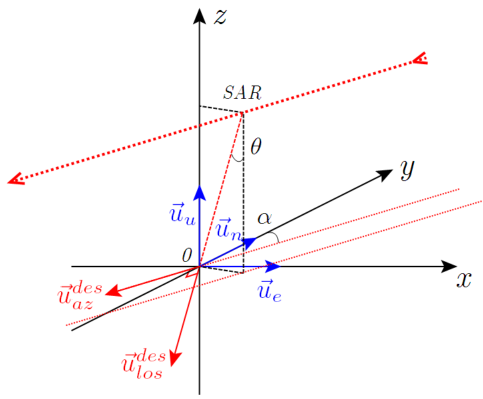

Fig. 12. Configuration of ground $\mathcal{B}_{3d} = (O, \vec{u}_e, \vec{u}_n, \vec{u}_u)$ and SAR $\mathcal{B}_{SAR}^{des} = (O, \vec{u}_{los}^{des}, \vec{u}_{az}^{des})$ basis in the descending track. The angles θ and α represent, respectively, the incidence angle and the azimuthal direction angle.

Descending track:

The coordinates of the $\vec{u}_{los}^{des}$ and the $\vec{u}_{az}^{des}$ vectors in the ground basis $\mathcal{B}_{3d}$ are respectively:

$$\vec{u}_{los}^{des} = \begin{bmatrix} -sin(\theta)\, cos(\alpha) \\ sin(\theta)\, sin(\alpha) \\ -cos(\theta) \end{bmatrix} \quad and \quad \vec{u}_{az}^{des} = \begin{bmatrix} -sin(\alpha) \\ -cos(\alpha) \\ 0 \end{bmatrix} \tag{8}$$

According to Eq. 7 and Eq. 8 the projection of the *in-situ* measurement in the SAR basis $\mathcal{B}_{SAR}^{des}$ in descending configuration is:

$$\vec{V}_{gndtoSAR}^{des} = \begin{bmatrix} -sin(\theta)\, cos(\alpha)\,.V_e + sin(\theta)\, sin(\alpha)\,.V_n - cos(\theta)\,.V_u \\ -sin(\alpha)\,.V_e - cos(\alpha)\,.V_n \end{bmatrix} \tag{9}$$

Ascending track:

The coordinates of the $\vec{u}_{los}^{asc}$ and the $\vec{u}_{az}^{asc}$ vectors in the ground basis $\mathcal{B}_{3d}$ are respectively:

$$\vec{u}_{los}^{asc} = \begin{bmatrix} sin(\theta)\, cos(\alpha) \\ sin(\theta)\, sin(\alpha) \\ -cos(\theta) \end{bmatrix} \quad and \quad \vec{u}_{az}^{asc} = \begin{bmatrix} -sin(\alpha) \\ cos(\alpha) \\ 0 \end{bmatrix} \tag{10}$$

According to Eq. 7 and Eq. 10 the projection of the *in-situ* measurement in the SAR basis $\mathcal{B}_{SAR}^{asc}$ in ascending configuration is:

$$\vec{V}_{gndtoSAR}^{asc} = \begin{bmatrix} sin(\theta)\, cos(\alpha)\,.V_e + sin(\theta)\, sin(\alpha)\,.V_n - cos(\theta)\,.V_u \\ -sin(\alpha)\,.V_e + cos(\alpha)\,.V_n \end{bmatrix} \tag{11}$$

ACKNOWLEDGMENT

The authors wish to thank the French Research Agency (ANR) for supporting this work through the EFIDIR project (ANR-2007-MCDC0-04, http://www.efidir.fr), the German Aerospace Agency (DLR) for the TerraSAR-X images (project MTH0232, http://sss.terrasar-x.dlr.de), the LGGE laboratory, the “Société d’Electricité d’Emosson SA” for the meteorological data and in situ measurements and the GlaRiskAlp project (projet simple Alcotra n°56). The GPS receivers have been provided by the French national GPS park (INSU-GPS). The authors would also like to thank the anonymous reviewers for providing precise comments and useful advice on this paper.

REFERENCES

[1] A. Kääb, *Remote sensing of Mountain glaciers and permafrost creep*. Geographisches Institut der Universität Zürich, 2004.

[2] E. Berthier, H. Vadon, D. Baratoux, Y. Arnaud, C. Vincent, K. Feigl, F. Rémy, and B. Legrésy, “Mountain glaciers surface motion derived from satellite optical imagery,” *Remote Sensing Environ.*, vol. 95, no. 1, pp. 14–28, 2005.

[3] F. Chatelain, J. Tourneret, J. Inglada, and A. Ferrari, “Bivariate gamma distributions for image registration and change detection,” *IEEE Trans. on Image Processing*, vol. 16, no. 7, pp. 1796–1806, 2007.

[4] N. Longépé, S. Allain, L. Ferro-Famil, E. Pottier, and Y. Durand, “Snowpack characterization in mountainous regions using C-band sar data and a meteorological model,” *IEEE Transactions on Geoscience and Remote Sensing*, vol. 47, no. 2, pp. 406–418, 2009.

[5] R. Michel, J. Avouac, and J. Taboury, “Measuring ground displacements from SAR amplitude images: application to the Landers earthquake,” *Geophysical Research Letters*, vol. 26, no. 7, p. 875878, 1999.

[6] T. Strozzi, A. Luckman, T. Murray, U. Wegmuller, and C. Werner, “Glacier motion estimation using SAR offset-tracking procedures,” *IEEE Transactions on Geoscience and Remote Sensing*, vol. 40, no. 11, pp. 2384–2391, 2002.

[7] F. Serafino, “SAR image coregistration based on isolated point scatterers,” *IEEE Geoscience and Remote Sensing Letters*, vol. 3, no. 3, pp. 354–358, 2006.

[8] K. Nakamura, K. Doi, and K. Shibuya, “Estimation of seasonal changes in the flow of Shirase glacier using JERS-1/SAR image correlation,” *Polar Science*, vol. 1, no. 2-4, pp. 73–83, 2007.

[9] E. Erten, A. Reigber, and O. Hellwich, “Glacier velocity monitoring by maximum likelihood texture tracking,” *IEEE Transactions on Geoscience and Remote Sensing*, vol. 47, no. 2, pp. 394–405, 2009.

[10] D. Massonnet and K. Feigl, “Radar interferometry and its application to changes in the Earth’s surface,” *Rev. Geophys.*, vol. 36, no. 4, pp. 441–500, 1998.

[11] I. R. Joughin, R. Kwok, and M. A. Fahnestock, “Interferometric estimation of three-dimentional ice-flow using ascending and descending passes,” *IEEE Transactions on Geoscience and Remote Sensing*, vol. 36, pp. 25–37, 1998.

[12] K. E. Mattar, P. W. Vachon, D. Geudtner, A. L. Gray, I. G. Cumming, and M. Brugman, “Validation of alpine glacier velocity measurements using ERS tandem-mission SAR data,” *IEEE Transactions on Geoscience and Remote Sensing*, vol. 36, pp. 974–984, 1998.

[13] E. Trouvé, G. Vasile, M. Gay, L. Bombrun, P. Grussenmeyer, T. Landes, J. Nicolas, P. Bolon, I. Petillot, A. Julea, L. Valet, J. Chanussot, and M. Koehl, "Combining airborne photographs and spaceborne SAR data to monitor temperate glaciers. Potentials and limits," *IEEE Transactions on Geoscience and Remote Sensing*, vol. 45, no. 4, pp. 905–923, 2007.

[14] T. Landes, M. Gay, E. Trouvé, J.-M. Nicolas, L. Bombrun, G. Vasile, and I. Hajnsek, "Monitoring temperate glaciers by high resolution Pol-Insar data: first analysis of Argentière E-SAR acquisitions and in-situ measurements," *IEEE Geoscience and Remote Sensing Symposium Proceedings, IGARSS'07, Barcelona, Spain*, 2007.

[15] I. Pétillot, E. Trouvé, P. Bolon, A. Julea, Y. Yan, M. Gay, and J.-M. Vanpé, "Radar-coding and geocoding lookup tables for the fusion of GIS and SAR data in mountain areas," *IEEE Geoscience and Remote Sensing Letters*, vol. 7, no. 2, pp. 309–313, 2010.

[16] R. Werninghaus and S. Buckreuss, "The TerraSAR-X mission and system design," *IEEE Transactions on Geoscience and Remote Sensing*, vol. 48, no. 2, pp. 875–878, 2010.

[17] D. Floricioiu and H. Rott, "Seasonal and short-time variability of multifrequency, polarimetric radar backscatter of alpine terrain from SIR-C/X-SAR and airsar data," *IEEE Transactions on Geoscience and Remote Sensing*, vol. 39, no. 12, pp. 2634–2648, 2001.

[18] D. Floricioiu, M. Eineder, H. Rott, and T. Nagler, "Velocities of major outlet glaciers of the Patagonia icefield observed by TerraSAR-X," in *IGARSS '08, Boston, Massachusetts, USA*, vol. IV, 2008, pp. 347–350.

[19] V. Kumar, G.Venkataraman, and Y. S. Rao, "SAR interferometry and speckle tracking approach for glacier velocity estimation using ERS-1/2 and TerraSAR-X spotlight high resolution data," in *Geoscience and Remote Sensing Symposium, IGARSS 2009, Capetown, South Africa*, July 2009.

[20] "EFIDIR: ANR project MDCO 2007," http://www.efidir.fr.

[21] B. Zitová and J. Flusser, "Image registration methods: a survey," *Image and Vision Computing*, vol. 21, no. 11, pp. 977–1000, 2003.

[22] T. Herring, R. King, and S. M. Clusky, "GAMIT reference manual," Department of Earth, Atmospheric and Planetary Sciences, Massachusetts Institute of Technology, GPS Analysis at MIT Release 10.35, 2006.

[23] D. Quincey, L. Copland, C. Mayer, M. Bishop, A. Luckman, and M. Belò, "Ice velocity and climate variations for Baltoro glacier, Pakistan," *Journal of Glaciology*, vol. 55, no. 194, 2009.

[24] "State control over management of the Pays de Savoie data," http ://www.rgd7374.fr.

[25] D. Schubert, M. Jehle, D. Small, and E. Meier, "Influence of atmospheric path delay on the absolute geolocation accuraccy of TerraSAR-X high-resolution products," *IEEE Transactions on Geoscience and Remote Sensing*, vol. 48, no. 2, pp. 751–758, 2010.

TABLE II

COMPARISON BETWEEN GPS N°1 AND REMOTE-SENSING POINT TARGET DISPLACEMENT MEASUREMENTS ON THE ARGENTIÈRE GLACIER. GPS DISPLACEMENTS ARE PROJECTED IN SAR GEOMETRY. THE MAGNITUDE (MAG.) AND THE ORIENTATION (ORI.) OF DISPLACEMENT VECTORS ARE IN CM/DAY AND DEGREE RESPECTIVELY. THE MAGNITUDE AND ORIENTATION IN PARENTHESIS CORRESPOND TO THE MAGNITUDE OF ERROR VECTOR AND THE ORIENTATION DIFFERENCE BETWEEN SAR VECTORS AND GPS VECTORS.

Orbit - Time series	**Dates**	**GPS n°1**		**CR (2767 m)**					
				sinc		**ZNCC**		***UML***	
		Mag.	**Ori.**	**Mag.**	**Ori.**	**Mag.**	**Ori.**	**Mag.**	**Ori.**
Des.	**2008-09-29/2008-10-10**	8.5	206.8°	*6.6*	*206.9°*	*7.2*	*209.6°*	*7.7*	*190.0°*
				(1.9)	*(-0.1°)*	*(1.3)*	*(-2.8°)*	*(2.5)*	*(16.8°)*
Autumn	**2008-10-10/2008-10-21**	8.5	206.3°	*8.9*	*214.9°*	*9.1*	*208.8°*	*12.1*	*207.1°*
2008				*(1.4)*	*(-8.6°)*	*(0.7)*	*(-2.5°)*	*(3.6)*	*(-0.8°)*
	Mean	8.5	206.0	*7.8*	*210.9°*	*8.1*	*209.2°*	*9.9*	*198.6°*
				(1.0)	*(-4.9°)*	*(0.8)*	*(-3.2°)*	*(1.5)*	*(7.4°)*
	RMS error			*1.6*	*6.0°*	*1.1*	*2.6°*	*3.1*	*11.9°*
Des.	**2009-05-29/2009-06-09**	12.8	204.3°	*11.7*	*200.4°*	*11.6*	*199.8°*	*11.5*	*180.8°*
				(1.4)	*(3.9°)*	*(1.5)*	*(4.5°)*	*(5.1)*	*(23.5°)*
	2009-06-09/2009-06-20	11.8	206.6°	*9.2*	*202.8°*	*9.5*	*202.0°*	*10.8*	*210.5°*
Spring/				*(2.7)*	*(3.8°)*	*(2.4)*	*(4.6°)*	*(1.2)*	*(-3.9°)*
Summer	**2009-06-20/2009-07-01**	9.4	208.8°	*12.3*	*209.9°*	*10.3*	*204.4°*	*6.9*	*204.5°*
2009				*(3.0)*	*(-1.1°)*	*(1.2)*	*(4.4°)*	*(2.6)*	*(4.3°)*
	2009-07-01/2009-07-12	9.7	206.1°	*11.2*	*205.0°*	*10.4*	*201.9°*	*8.3*	*192.2°*
				(1.6)	*(1.1°)*	*(1.0)*	*(4.2°)*	*(2.5)*	*(13.9°)*
	Mean	10.9	206.4	*11.1*	*204.5°*	*10.4*	*202.0°*	*9.4*	*197.0°*
				(0.3)	*(1.9°)*	*(0.9)*	*(4.4°)*	*(2.8)*	*(9.4°)*
	RMS error			*2.3*	*2.8°*	*1.6*	*4.4°*	*3.2*	*13.9°*
Asc.	**2009-05-31/2009-06-11**	12.3	49.5°	*13.8*	*57.3°*	*14.0*	*57.8°*	*23.3*	*84.6°*
				(2.3)	*(-7.8°)*	*(2.5)*	*(-8.3°)*	*(15.0)*	*(-35.1°)*
	2009-06-11/2009-06-22	13.7	48.3°	*7.8*	*57.9°*	*8.0*	*63.3°*	*5.5*	*110.6°*
Spring/				*(6.1)*	*(-9.6°)*	*(6.2)*	*(-15.0°)*	*(12.1)*	*(-62.3°)*
Summer	**2009-06-22/2009-07-03**	11.5	46.5°	*10.5*	*34.6°*	*10.1*	*35.7°*	*26.8*	*79.6°*
2009				*(2.5)*	*(11.9°)*	*(2.4)*	*(10.8°)*	*(18.3)*	*(-33.1°)*
	2009-07-03/2009-07-14	11.5	44.8°	*14.8*	*46.0°*	*13.8*	*42.9°*	*23.9*	*1.7°*
				(3.3)	*(-1.2°)*	*(2.4)*	*(1.9°)*	*(17.4)*	*(43.1°)*
	Mean	12.2	47.3	*11.7*	*48.9°*	*11.5*	*49.9°*	*19.9*	*69.1°*
				(0.7)	*(-1.6°)*	*(1.0)*	*(-2.6°)*	*(4.9)*	*(-21.8°)*
	RMS error			*3.9*	*8.6°*	*3.8*	*10.2°*	*15.9*	*44.9°*
Total RMS error				*2.9*	*6.3°*	*2.6*	*7.1°*	*10.3*	*30.2°*

TABLE III

COMPARISON BETWEEN GPS N°3 AND REMOTE-SENSING POINT TARGET AND DISTRIBUTED TARGET DISPLACEMENT MEASUREMENTS ON THE ARGENTIÈRE GLACIER. GPS DISPLACEMENTS ARE PROJECTED IN SAR GEOMETRY. THE MAGNITUDE (MAG.) AND THE ORIENTATION (ORI.) OF DISPLACEMENT VECTORS ARE IN CM/DAY AND DEGREE RESPECTIVELY. THE MAGNITUDE AND ORIENTATION IN PARENTHESIS CORRESPOND TO THE MAGNITUDE OF ERROR VECTOR AND THE ORIENTATION DIFFERENCE BETWEEN SAR VECTORS AND GPS VECTORS.

Orbit - Time series	**Dates**	**GPS n°3**		**CR (2360 m)**		**Distributed target (2360 m)**			
				ZNCC		**ZNCC**		**UML**	
		Mag.	**Ori.**	**Mag.**	**Ori.**	**Mag.**	**Ori.**	**Mag.**	**Ori.**
Des. Spring/Summer 2009	**2009-08-14/2009-08-25**	16.4	195.2°	*21.6*	*200.7°*	22.4	214.5°	22.1	214.6°
				(5.5)	*(-5.5°)*	*(8.8)*	*(-19.3°)*	*(8.6)*	*(-19.4°)*
Asc.	**2009-07-14/2009-07-25**	19.3	65.6°	*14.4*	*55.7°*	16.5	*63.9°*	25.2	*35.7°*
				(5.6)	*(9.9°)*	*(2.8)*	*(1.7°)*	*(12.8)*	*(29.9°)*
	2009-07-25/2009-08-05	18.6	68.7°	*19.1*	*67.6°*	*22.5*	*79.2°*	*21.8*	*81.9°*
Spring/				*(0.7)*	*(1.1°)*	*(5.4)*	*(-10.4°)*	*(5.6)*	*(-13.2°)*
Summer	**2009-08-05/2009-08-16**	9.4	51.9°	*11.0*	*64.3°*	*17.7*	*73.6°*	*18.5*	*75.9°*
2009				*(2.7)*	*(-12.4°)*	*(9.6)*	*(-21.6°)*	*(10.7)*	*(-24.0°)*
	2009-08-16/2009-08-27	10.1	60.7°	*13.6*	*59.9°*	*17.3*	*65.3°*	*16.7*	*64.2°*
				(3.5)	*(0.8°)*	*(7.3)*	*(-4.6°)*	*(6.6)*	*(-3.5°)*
	Mean	14.3	61.7°	*14.5*	*61.8°*	*18.5*	*70.5°*	*20.5*	*64.4°*
				(0.1)	*(-0.1°)*	*(5.5)*	*(-8.8°)*	*(5.5)*	*(-2.7°)*
	RMS error			*3.6*	*7.9°*	*6.8*	*12.3°*	*9.4*	*20.3°*
Total RMS error				*4.1*	*7.5°*	*7.2*	*14.0°*	*9.2*	*20.3°*